SCIENCE CHINA
Physics, Mechanics & Astronomy

• Research Paper •

September 2011 Vol.54 No.9: 1702–1709
doi: 10.1007/s11433-011-4446-2

Experimental study of a supersonic turbulent boundary layer using PIV

HE Lin*, YI ShiHe, ZHAO YuXin, TIAN LiFeng & CHEN Zhi

College of Aerospace and Material Engineering, National University of Defense Technology, Changsha 410073, China

Received November 2, 2010; accepted March 8, 2011; published online July 26, 2011

Particle image velocimetry was applied to the study of the statistical properties and the coherent structures of a flat plate turbulent boundary layer at Mach 3. The nanoparticles with a good flow-following capability in supersonic flows were adopted as the tracer particles in the present experiments. The results show that the Van Driest transformed mean velocity profile satisfies the incompressible scalings and reveals a log-law region that extends to y/δ=0.4, which is further away from the wall than that in incompressible boundary layers. The Reynolds stress profiles exhibit a plateau-like region in the log-law region. The hairpin vortices in the streamwise-wall-normal plane are identified using different velocity decompositions, which are similar to the results of the flow visualization via NPLS technique. And multiple hairpin vortices are found moving at nearly the same velocity in different regions of the boundary layer. In the streamwise-spanwise plane, elongated streaky structures are observed in the log-law region, and disappear in the outer region of the boundary layer, which is contrary to the flow visualization results.

PIV, turbulence, supersonic boundary layer, hairpin vortices, statistical property, coherent structures

PACS: 47.40.ki, 47.27.nb, 47.80.cb

Over the past few decades, considerable attention has been given to the study of compressible turbulence. However, due to the complexity of the compressible turbulent flows, a large amount of work has been devoted to the study of simpler flows, such as flat-plate turbulent boundary layer, which has helped to improve our understanding of the compressible turbulence. Until recently, considerable progress has been made in studying incompressible turbulent boundary layers. In contrast, the progress in compressible flows, especially in supersonic flows, is still insufficient owing to the inherent difficulties both in experiments and in numerical simulations.

In experimental studies, hot-wire anemometry (HWA) is the most common measurement technique for obtaining turbulence data in supersonic flows, but the uncertainty levels are considerably higher than that in subsonic flows, as reported by Smits and Dussauge [1]. Particle image velocimetry (PIV) and laser Doppler velocimetry (LDV) have become useful tools for studying supersonic flows in the last two decades [2,3], but they are both limited by the particle response times and the seeding difficulties in high-speed flows. Although currently limited to relatively low Reynolds numbers, the numerical simulation methods such as direct numerical simulations (DNS) and large eddy simulation (LES) have become more and more important in the study of compressible turbulence. Recently, a few numerical simulations of supersonic turbulent boundary layers have been performed. Pirozzoli et al. and Gatski et al. performed DNS of a spatially evolving flat plate boundary layer at Mach 2.25 [4,5]. Huang et al. analyzed the properties of a supersonic turbulent boundary layer at Mach 4.5 using temporal mode DNS [6], and investigated the coherent structures in the wall region [7]. The simulation of a Mach 3 adiabatic turbulent boundary layer can be found in ref. [8] using LES, and ref. [9] using DNS. A review of the studies of supersonic turbulent boundary layers can be

*Corresponding author (email: helin.101sys@gmail.com)

found in ref. [10].

According to Morkovin's hypothesis [11], for moderate Mach numbers, compressibility effects do not influence the dynamic behavior of turbulence directly, and the principal effect of high speeds is felt through the change in fluid properties. Experimental data reported by Smits and Dussauge [10] also confirm that supersonic boundary layers at zero pressure gradient exhibit close similarities with incompressible ones. However, recent experimental work has indicated that the turbulent structures of subsonic and supersonic boundary layers are different in some ways [12]. Therefore, further investigations of the supersonic turbulent boundary layer are necessary.

In this paper, the velocity measurements of a zero- pressure-gradient turbulent boundary layer at Mach 3 have been performed using PIV technique. The nanoparticles were adopted as the tracer particles to provide higher accuracy measurements, due to its good flow-following capability in supersonic flows. The statistical properties, such as mean streamwise velocity profile, the distribution of the Reynolds stresses and the turbulent Mach number, are presented. And the coherent structures are identified using these PIV data in both the streamwise-wall-normal plane and streamwise-spanwise plane. These structures are compared with the flow visualization results via NPLS technique [13], which would provide a better understanding of supersonic turbulent boundary layers.

1 Flow facility

The experiments were performed in the KD-03 supersonic wind tunnel of the Aerodynamics Laboratory at National University of Defense Technology. The test section dimensions are 120(H)×100(W) mm^2. In the present study, the wind tunnel was operated at a nominal Mach number of 3 with a stagnation pressure of 101 kPa and stagnation temperature of 300 K. The test boundary layer was developed in a nominally zero pressure gradient along the wall of the test section, with transition occurring naturally upstream in the nozzle. The experimental parameters are given in Table 1.

2 PIV technique

In order to improve the flow-following ability of the tracer particles in supersonic flows, titanium dioxide (TiO_2) particles with a nominal diameter of 20 nm and a bulk density of approximately 300 kg/m^3 were adopted as the tracer particles in the present PIV experiments. The particle relaxation time across an oblique shock wave has been previously estimated to be τ_p=0.15 μs [14], and the corresponding Stokes number (based upon a flow time scale δ/U_∞=16.5 μs) was S_t=0.009 (<0.05), indicating that the chosen particles met the flow-following criteria suggested by Samimy and Lele [15].

Table 1 Experimental parameters

Parameter	Quantity
M_∞	3
T_0 (K)	300
P_0 (kPa)	101.0
Re (m^{-1})	7.49×10^6
U_∞ (m/s)	620

The seeded flow was illuminated by a Q-switched dual cavity Nd:YAG laser, with 350 mJ pulsed energy and a 6 ns pulse duration at wavelength 532 nm. The laser beam is oriented by an articulated arm and focused as a uniform sheet by a cylindrical lens. The particle images were recorded by a 12-bit CCD camera with a resolution of 2048×2048 pixels. In the present experiments, the boundary layer is to be described in a Cartesian coordinate system (x, y, z), where x, y and z denote the streamwise, wall-normal and spanwise directions, respectively. The respective velocities are denoted by u, v and w. The instantaneous velocity fields were measured in a streamwise-wall-normal (xy) plane along the spanwise centerline of the test section, and two streamwise-spanwise (xz) planes at y/δ =0.2 and 0.8, respectively. The field of view in the xy-plane was about 35 mm × 35 mm, with a spatial resolution of approximately 17 μm/pixel. In the xz-planes, the fields of view were 80 mm× 40 mm, and the spatial resolution was 40 μm/pixel. The time delay between the two laser pulses was 0.5 μs, which allowed a particle displacement in the free stream of approximately 0.3 mm (approximately 18 pixels in the xy-plane and 7.5 pixels in the xz-plane). An ensemble of 300 particle images in the xy-plane was acquired to study the statistical properties of the boundary layer. Each image pair was interrogated using a 64×32-pixel window with an overlap factor of 50%. This resulted in a window size of 1.1×0.56 mm^2, and a vector spacing of about 0.28 mm (approximately 0.03δ or 15 viscous wall units) in the wall-normal direction. Another 200 particle images were acquired in each xz-plane to study the instantaneous structures of the boundary layer, using a window of size 32×16 pixels (1.3×0.64 mm^2) with an overlap factor of 50%.

3 The statistical properties of the boundary layer

The turbulent boundary layer properties are summarized in Table 2, where δ^* and θ are the compressible displacement thickness and momentum thickness, respectively. The temperature profile was calculated from the adiabatic Crocco-Busemann relation with a constant recovery factor r=1. The density profile was deduced from the temperature profile, assuming constant pressure across the boundary layer. The

Table 2 Turbulent boundary layer properties

Parameter	Quantity
δ_{99} (mm)	10.2
δ^* (mm)	3.66
θ (mm)	0.68
δ^*/δ_{99}	0.36
θ/δ_{99}	0.067
$H=\delta^*/\theta$	5.38
Re_θ	5100
Re_δ	76500
u_τ (m/s)	29.9
C_f	1.70×10^{-3}

friction velocity u_τ was estimated using the method reported by Kendall and Koochesfahani [16].

3.1 Mean properties

The mean streamwise velocity u^+, transformed using the method of van Driest [17], is plotted versus y^+ in Figure 1. The superscript ($^+$) indicates normalization using u_τ for the velocity and v_w/u_τ for the length, where u_τ is the friction velocity and v_w is the kinematic viscosity at the wall. The comparison of the mean compressible streamwise velocity profile with Spalding's universal velocity profile [18] and the standard log law profile (with κ=0.41 and C=5.1) is shown in Figure 1(a). The result shows that the Van Driest transformed velocity satisfies the incompressible scaling and exhibits a log-law behavior in the range between y^+=30 ($y/\delta\approx0.05$) and y^+=220 ($y/\delta\approx0.4$). Considering that the log-law region is usually y/δ<0.3 in incompressible boundary layers, this region seems to extend farther in the wall-normal direction in the present boundary layer. However, this result is consistent with the previous experimental findings of Robinson [19], Kistler [20] and Ganapathisubramani [21], where the log-law region of supersonic boundary layers was extended to $y/\delta\leqslant0.6$. The van Driest transformed velocity profile associated with other numerical simulation results [5,8,9,22] is plotted in Figure 1(b). The present result shows a good agreement with the DNS data for $30<y^+<330$ ($0.05<y/\delta<0.6$), despite a large difference between the present data and the LES result. The discrepancies between the present data and the numerical simulation results in the near-wall region may be due to the measurement errors of PIV. However, the discrepancies in the outermost region are most likely due to the difference in the Reynolds numbers. To the authors' knowledge, no numerical simulation data exist for a Mach 3 turbulent boundary layer at similar experimental Reynolds numbers.

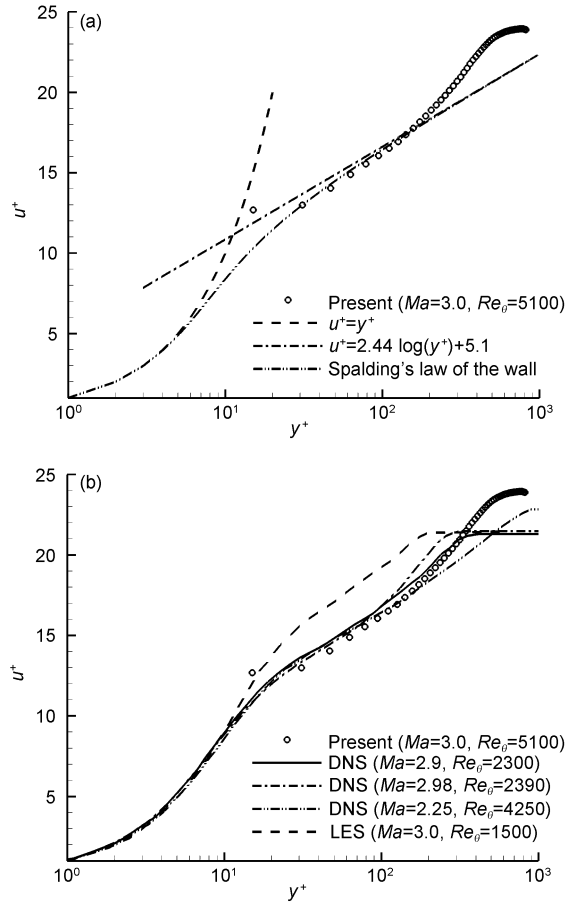

Figure 1 Van Driest transformed mean velocity profile. (a) Compared with Spalding's universal velocity profile [18] and the standard log law profile; (b) compared with other numerical simulation results [5,8,9,22].

3.2 Turbulent properties

The turbulent Mach number defined by the root-mean-square (RMS) of streamwise velocity fluctuations and the local mean speed of sound ($M_t=\sqrt{\overline{u'}}/\overline{a}$) is plotted in Figure 2, which is found to be smaller than 0.23 across the boundary layer. This result is followed by the Morkovin's hypothesis that for turbulent boundary layers on a flat plate with freestream Mach number smaller than 4, M_t is nowhere larger than 0.3. Morkovin also suggested that the compressibility effect is small and can be neglected if the turbulent Mach number is smaller than its threshold value M_t =0.3. Therefore, the compressibility effect in the present supersonic turbulent boundary layer can be neglected, and the turbulent properties can be compared to those of incompressible boundary layers. However, the log-law region extending farther in the wall-normal direction in the present study is probably due to the large velocity gradient in supersonic boundary layers. And the fact that the intermittency profile in a supersonic boundary layer is fuller than the corresponding subsonic profile may be another explanation, according to Smits et al. [12].

The velocity fluctuations of the boundary layer are shown in Figure 3, where <·> denotes the RMS quantity. In

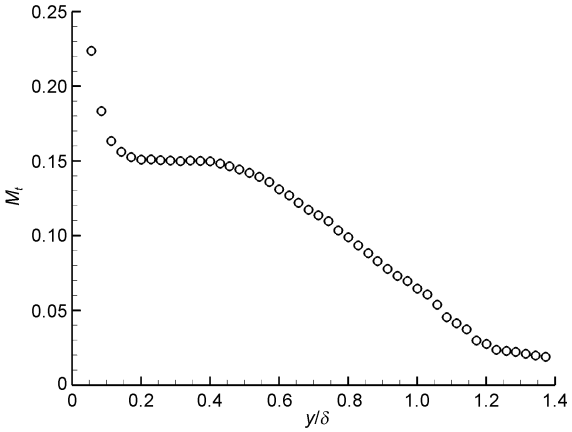

Figure 2 Distribution of the turbulent Mach number.

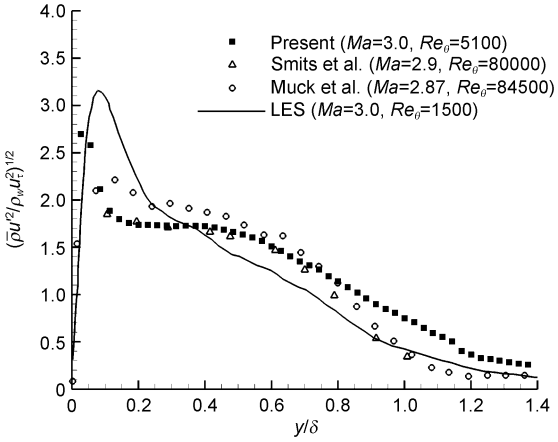

Figure 4 Distribution of the Reynolds normal stresses.

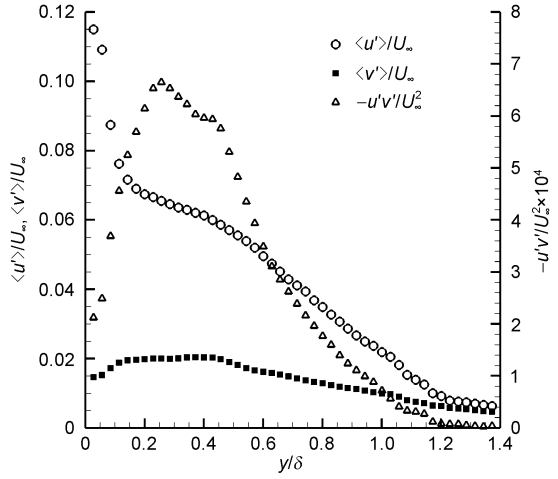

Figure 3 Velocity fluctuations of the turbulent boundary layer.

the present experiments, the freestream turbulent level does not exceed 2% derived from these results. The maximum value of $-\overline{u'v'}$ is $0.07\%U_\infty$ at approximately y/δ=0.26, while the maximum value of $\langle v'\rangle$ is 0.21%, keeping almost constant in the range $0.2<y/\delta<0.4$. Due to the measurement errors of PIV in the near-wall region, the maximum value of $\langle u'\rangle$ is unreliable plotted in Figure 3. Considering that the large-scale structures could cause larger velocity fluctuations, one can infer that the large-scale coherent structures may exist in the region where the velocity fluctuations are large. Therefore, the region $y/\delta<0.4$, which belongs to the log-law region, is believed to be the main region of the existence of the large-scale coherent structures in the present boundary layer.

The Reynolds stresses $\overline{\rho u'^2}$ and $\overline{\rho u'v'}$, normalized using the wall shear stress $\tau_w = \rho_w u_\tau^2$, are shown in Figure 4 and 5 respectively, where the results of Urbin et al. [8], Smits et al. [12] and Muck et al. [23] are also displayed. Due to a maximum absolute uncertainty of about 0.1 pixel (here, is equivalent to 3.5 m/s) on the displacement calculated from the correlation peak detection in the PIV measurements, the relative uncertainties of the nondimensional Reynolds stresses in the present experiments are found greater than 20% beyond y/δ=0.8. This may explain the relatively large discrepancies between the present Reynolds stress profiles and the other results near the edge of the boundary layer. Nevertheless, the present Reynolds normal stress profile shows a good agreement with the experimental results of Muck et al. [23] and Smits et al. [12] for $0.4<y/\delta<0.8$, despite a significantly higher Reynolds number Re_θ in their flows. The LES result displays a relatively lower value than the experimental data for $y/\delta>0.4$, which may be due to the low-Reynolds-number effects. In the near-wall region ($y/\delta<0.2$), the present data show a good agreement with the experimental data of Smits, but a relative high value of the experimental data of Muck is found. However, large discrepancies remain between the experimental data and the LES result. As shown in Figure 5, the agreement of the Reynolds shear stress profiles is excellent for $0.4<y/\delta<0.8$, but the peak value of the present data is lower than other results. The reason for the discrepancies between the experimental data and LES result may be attributed to the differences in Reynolds number, although the experimental measurements in the near-wall region are subject to considerable uncertainty. Besides, a plateau-like region between y/δ=0.2 and 0.4 in the present Reynolds normal stress profile, and between y/δ=0.25 and 0.45 in the Reynolds shear stress profile can be observed respectively. Such feature is not found in the LES and Muck's results, but similar feature in the Reynolds normal stress profile was reported by Ganapathisubramani in the region between y/δ=0.4 and 0.6. Whether it is a new feature of supersonic turbulent boundary layers is not clear yet, and awaits further experimental and numerical studies.

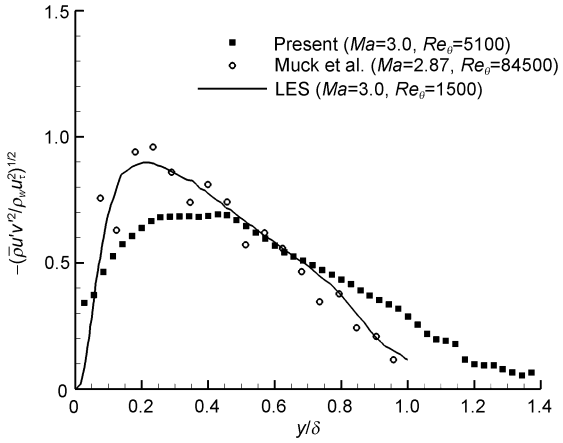

Figure 5 Distribution of the Reynolds shear stresses.

4 Instantaneous structures of the turbulent boundary layer

4.1 Instantaneous structures in the *xy*-plane

The hairpin vortex, first introduced by Theodorsen [24], is now widely accepted to be a primary feature of turbulent boundary layers. The signature pattern of the hairpin in the streamwise velocity field consists of a spanwise vortex core (as the head of a hairpin) located above a region of a VITA event [25]. Here, the VITA event, as defined by Blackwelder and Kaplan [26], represented the shear layer caused by the hairpins. This signature pattern has been commonly used to identify the hairpin vortices in incompressible boundary layers [25]. Considering the fact that, in the PIV measurements of supersonic flows, the time delay between each image pair must be very short (here Δt=0.5 μs), thus the rotations of the spanwise vortices would be very small during this time delay. As a result, the spanwise vorticity calculated from the instantaneous velocity is unreliable, and can not represent the head of the hairpin correctly. Therefore, only the VITA event can be used to detect the hairpin signature pattern in the velocity fields of a supersonic boundary layer. Although the hairpins inferred in this way may introduce some uncertainty, this can still provide a reasonable description of the hairpin vortices in the present boundary layers.

In this paper, the VITA events are detected using Galilean decomposition of the instantaneous velocity vector field. In Figures 6(a)–6(c), the velocity vector field is shown after subtracting convection velocities U_c = 0.6U_∞, 0.8U_∞ and 1.0U_∞ respectively, and the VITA events are indicated by the solid black line. Following the criteria adopted above, the hairpin vortices are interpreted to exist at the location of these black lines. As shown in Figure 6(a), the small-scale hairpins can be found in the near-wall region (y/δ<0.1), moving at a relatively low convection velocity (U_c = 0.6U_∞),

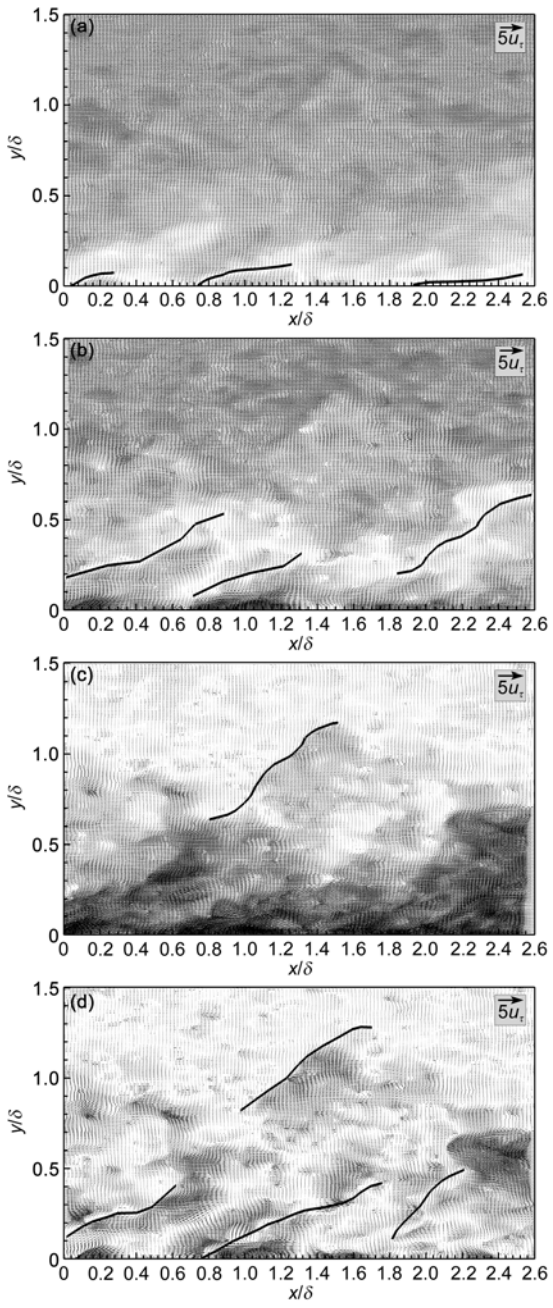

Figure 6 Instantaneous velocity vector field shown in the *xy*-plane using several different types of vector decomposition. (a) Vectors viewed in a frame-of-reference convecting at U_c = 0.6U_∞; (b) vectors viewed in a frame-of-reference convecting at U_c = 0.8U_∞; (c) vectors viewed in a frame-of-reference convecting at U_c = 1.0U_∞; (d) Reynolds decomposed fluctuating vectors. The flow is from left to right.

the inclination angle ranges from 5° to 15°. In the log-law region (0.1<y/δ<0.4), large-scale hairpins can be identified in Figure 6(b), with a higher convection velocity at U_c = 0.8U_∞. The angle of inclination of the hairpins increases to 20°–30°. In the outer region of the boundary layer (y/δ>0.6), a larger-scale hairpin structure with an inclination angle at approximately 40° is seen in Figure 6(c), which is moving

at nearly the free stream velocity. It should be noticed that, using the Galilean decomposition, only the hairpin vortices moving with the selected convection velocity can be observed, and the hairpin vortices are randomly distributed in different regions of the boundary layer using different instantaneous velocity vector fields. Reynolds decomposition by subtracting the averaged velocity field from the instantaneous velocity field is another vector decomposition method used in this paper. Figure 6(d) shows the Reynolds decomposition of the velocity field, and the similar hairpin structures with nearly the same locations in Figures 6(b) and 6(c) can be identified. Although the Reynolds decomposition can detect the hairpin vortices with different convection velocities, the hairpin structures in the near-wall region as shown in Figure 6(a) are not observed. This may probably be due to the large shear of streamwise velocity in this region, and such structures are distorted by the Reynolds decomposition. In spite of the different velocity decomposition used here, multiple hairpins, propagating at nearly the same streamwise velocity, can be observed throughout the boundary layer. Although there is only one hairpin vortex observed in Figure 6(c), multiple hairpins, moving with the velocity equal to the free stream velocity in the outer region of the boundary layer, can be identified in other instantaneous velocity vector fields. These structures can be regarded as the hairpin packets as proposed by Adrian et al. [25].

The flow visualization of the present turbulent boundary layer in the *xy*-plane is shown in Figure 7 using NPLS technique. The field of view is nearly the same as the PIV measurements, and the flow is from left to right. Due to the complexity of the real flow, it may be difficult to interpret the coherent structures observed in this NPLS image. However, some inclined structures indicated by white arrows can be identified in this picture. In the near-wall, these structures are small in size, and inclined at 5–10° to the wall. But in the region farther away from the wall, the size of these structures increases, with the growth angle less than 45°. Such structures can also be observed at the edge of the boundary layer. These inclined structures share similar features of the shear layers of the hairpin vortices observed in Figure 6. According to the hairpin model, a shear layer is terminated in a region of rolled-up spanwise vorticity, which is interpreted to the head of a hairpin vortex. If these inclined structures observed in the NPLS image are assumed to the shear layer of the hairpins in the real flow, the spanwise vorticity will be found downstream along each shear layer. In the NPLS image, some circle-like structures indicated by black arrows can be observed, which are believed to be the heads of the hairpin vortices here. Considering the fact that the hairpin vortices in real flows are variations of a common basic flow structure at different stages of evolution, this may explain why the heads of the hairpins found in NPLS image are in the form of different sizes and shapes. Nevertheless, the heads of the hairpins are not found in the log-law region and the near-wall region in the NPLS image, and this may be due to a large deformation of the structures in this region, where the velocity shear is strong, and the relatively regular structures can not be identified. However, whether these inclined structures stand for the shear layers of the hairpin vortices needs further identification, it seems to be the most probable explanation in the present situation, on the basis of the hairpin model.

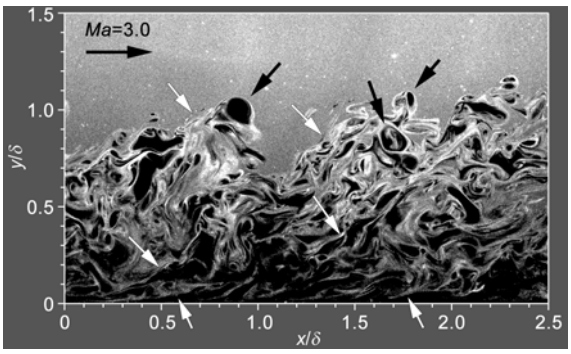

Figure 7 NPLS image of the present turbulent boundary layer in the *xy*-plane, and the flow is from left to right.

4.2 structures in the *xz*-plane

In this paper, the PIV measurements at two wall-normal locations have been performed to study the instantaneous structures of the boundary layer in the *xz*-plane. One was selected at y/δ=0.2(y^+=107) to identify the coherent structures in the log-law region. Another was selected at y/δ=0.8 (y^+=430) to study the structures in the outer region of the boundary layer. Here, the streamwise velocity fluctuations (u') instead of the velocity vector fields are selected, which would exhibit some easily observed features of the boundary layer.

The contours of the u', normalized by the friction velocity u_τ, are shown in Figure 8, and the flow is from left to right. At the wall-normal location of y/δ=0.2, the streamwise velocity fluctuation exhibits long streaks along the flow direction with a width of approximately 0.5–1.0δ, and a meandering feature of these structures can also be observed as shown in Figure 8(a). The length of these streaks is larger than 7.6δ (the length of the field of view), because they extend beyond the full field of view. Compared with other instantaneous velocity fields, these long streaks are distributed randomly in space. Similar structures can be found in both the experimental measurements [27] and numerical simulations [9] at supersonic conditions. However, the width and length of these structures are found in various sizes in the previous studies. In the outer region of the boundary layer at y/δ=0.8, these long streaks disappear and irregular structures are observed, as shown in Figure 8(b). According to the induction of a hairpin vortex, the region between the two legs contains negative velocity fluctuations and the zones on either side of the legs have positive veloc-

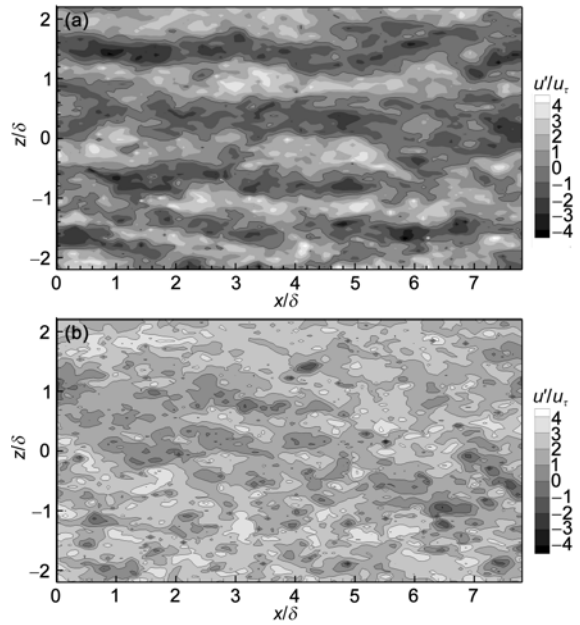

Figure 8 The contours of the streamwise velocity fluctuations normalized by u_τ at (a) y/δ=0.2 and (b) y/δ=0.8. The flow is from left to right.

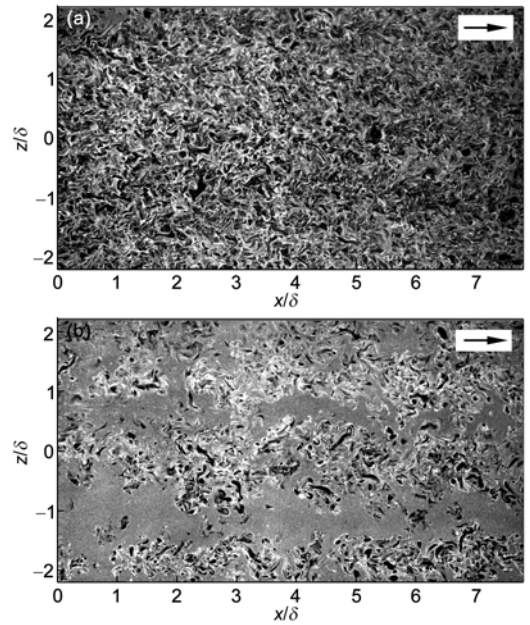

Figure 9 NPLS images of the present boundary layer in the *xz*-plane at (a) y/δ=0.2 and (b) y/δ=0.8.

ity, which could explain the formation of the uniform positive and negative velocity fluctuation regions observed in Figure 8(a). And because the legs of the hairpin vortices seldom exist in the outer region of the boundary layer, such structures disappear at y/δ=0.8 as seen in Figure 8(b).

Here, the flow visualization results are also provided to compare with the instantaneous structures observed in Figure 8. NPLS images of the present boundary layer in the *xz*-plane, with the same wall-normal location mentioned above, are presented in Figures 9(a) and 9(b) respectively. The field of view is the same as the PIV measurements and the flow is from left to right. To our surprise, such long streaks observed in Figure 8(a) can not be identified clearly at the same wall-normal location in Figure 9(a). On the contrary, elongated streaky structures are clearly observed in the outer region (y/δ=0.8) of the boundary layer as shown in Figure 9(b), which also extend beyond the full field of view with a meandering behavior. These structures are very similar to that observed in Figure 8(a), although the spanwise width increases to 1.0–2.0δ. The discrepancy of the structures observed between the PIV measurements and flow visualizations is most likely due to the basic principle of these two techniques. The PIV results reveal the velocity structures of the boundary layer, while the NPLS images exhibit the passive scalar structures (or qualitative density structures). Although some similar features between the velocity structures and the passive scalar structures are found in the *xy*-plane, a large difference between these two structures can be observed in the *xz*-plane. In the outer region of the boundary layer, the large-scale structures are found moving with a velocity equal to the free stream velocity, thus the velocity fluctuations at this location are small, and the elongated streaky structures observed in the NPLS image can not be identified in Figure 8(b). It is interesting that the coherent structures shown in Figure 9(a) look like a forest of hairpin, which represent the vortical structures, in a low-Reynolds number zero-pressure-gradient flat-plate boundary layer as reported by Wu et al. [28].

It should be noticed that the coherent structures in the real flows are so complicated that only one experimental technique such as PIV or NPLS can not interpret these structures clearly, and sometimes may lead to misunderstanding. Therefore, the combination of multiple methods would help to provide better physical understanding of supersonic turbulent boundary layers.

5 Conclusions

An experimental study of a flat-plate turbulent boundary layer at Mach 3 has been performed using PIV technique, where the nanoparticles with a good flow-following capability in supersonic flows were adopted as the tracer particles. The statistical properties and instantaneous structures in the streamwise-wall-normal (*xy*) plane and streamwise-spanwise (*xz*) plane are presented.

The Van Driest transformed mean velocity profile obeys the incompressible law-of-the-wall and shows a good agreement with previous numerical investigations, in spite of the difference in the Reynolds number Re_θ. The log-law region is found to extend from y/δ= 0.05 to 0.4, whose upper limit is farther away from the wall than that observed in incompressible boundary layers. The turbulent Mach number is found less than 0.3 across the boundary layer, thus the

compressible effect can be neglected in the present boundary layer according to Morkovin's hypothesis. The Reynolds stresses are consistent with previous studies, and a plateau-like region can be observed in the log-law region both in the profiles of the Reynolds normal stress and the Reynolds shear stress.

The hairpin vortices are identified in the *xy*-plane using the Galilean decomposition and the Reynolds decomposition of the velocity vector fields, which are similar to the structures observed in the flow visualization via NPLS. Multiple hairpin vortices are found moving at nearly the same velocity, and may be regarded as the hairpin packets. In the log-law region (at y/δ=0.2), the instantaneous streamwise velocity fluctuations in the *xz*-plane exhibit elongated streaky structures with a width of 0.5–1.0δ and a length beyond 7.6δ. These structures disappear in the outer region (at y/δ=0.8) of the boundary layer. On the contrary, in the NPLS images, these elongated streaky structures can not be found at y/δ=0.2, but can be observed with a larger width at y/δ=0.8. This discrepancy may be due to the difference of the velocity structures and passive scalar structures in the *xz*-plane, which implies that multiple measurement techniques should be combined together to provide a better understanding of supersonic turbulent boundary layers.

This work was supported by the National Basic Research Program of China (Grant No. 2009CB724100).

1 Smits A J, Dussauge J P. Hot-Wire Anemometry in Supersonic Flow. Chapter 5, AGARDograph 315, 1989
2 Johnson D, Rose W. Laser velocimeter and hot wire anemometer comparison in a supersonic boundary layer. AIAA J, 1975, 13: 512
3 Raffel M, Willert C, Wereley S, et al. Particle Image Velocimetry. 2nd ed. Springer, 2007
4 Pirozzoli S, Grasso F, Gatski T B. Direct numerical simulation and analysis of a spatially evolving supersonic turbulent boundary layer at *M*=2.25. Phys Fluids, 2004, 16: 530–545
5 Gatski T B, Erlebacher G. Numerical simulation of a spatially evolving supersonic turbulent boundary layer. NASA Tech. Memo, 2002-211934
6 Huang Z F, Zhou H, Luo J S. Direct numerical simulation of a supersonic turbulent boundary layer on a flat plate and its analysis. Sci China Ser G-Phys Mech Astron, 2005, 48: 626–640
7 Huang Z F, Zhou H, Luo J S. The investigation of coherent structures in the wall region of a supersonic turbulent boundary layer based on DNS database. Sci China Ser G-Phys Mech Astron, 2007, 50: 348–356
8 Urbin G, Knight D, Zheltovodov A A. Compressible Large Eddy Simulation using Unstructured Grid: Supersonic Turbulent Boundary Layer and Compression Corner. AIAA Paper, 1999, AIAA-99-0427
9 Ringuette M J, Wu M, Martin M P. Coherent structures in direct numerical simulation of turbulent boundary layers at Mach 3. J Fluid Mech, 2008, 594: 59–69
10 Smits A J, Dussauge J P. Turbulent Shear Layers in Supersonic Flow. 2nd ed. NewYork: Springer, 2006
11 Morkovin M V. Effects of compressibility on turbulent flows. Favre A, ed. Mécanique de la Turbulence. Paris: CNRS, 1962. 367–380
12 Smits A J, Spina E F, Alving A E, et al. A comparison of the turbulence structure of subsonic and supersonic boundary layers. Phys Fluids A, 1989, 1: 1865–1875
13 Zhao Y X, Yi S H, Tian L F, et al. Supersonic flow imaging via nanoparticles. Sci China Ser E-Tech Sci, 2009, 52: 3640–3648
14 Zhao Y X. Experimental investigation of spatiotemporal structures of supersonic mixing layer. Dissertation for the Doctoral Degree. Changsha: National University of Defense Technology, 2008
15 Samimy M, Lele S. Motion of particles with inertia in a compressible free shear layer. Phys Fluids, 1991, 3: 1915–1923
16 Kendall A, Koochesfahani M. A method for estimating wall friction in turbulent wall-bounded flows. Exp Fluids, 2008, 44: 773–780
17 van Driest E R. On Turbulent Flow near a Wall. Journal of the Aeronautical Sciences, 1956, 23: 1007–1011
18 Spalding D B. A single formula for the law of the wall. J Appl Mech, 1961, 28: 455–457
19 Robinson S K. Space-time correlation measurements in a compressible turbulent boundary layer. AIAA Paper, 1986, AIAA-1986-1130
20 Kistler A L. Fluctuation measurements in supersonic turbulent boundary layer. Phys Fluids, 1959, 2: 290–296
21 Ganapathisubramani B. Statistical properties of streamwise velocity in a supersonic turbulent boundary layer. Phys Fluids, 2007, 19: 098108
22 Wu M, Martin M P. Direct numerical simulation of supersonic turbulent boundary layer over a compression ramp. AIAA J, 2007, 45: 879–889
23 Muck K, Spina E, Smita A. Compilation of Turbulence Data for an 8 Degree Compression Comer at Mach 2.9. Report No. MAE-1642. April 1984
24 Theodorsen T. Mechanism of turbulence. In: Proceedings of the Second Midwestern Conference on Fluid Mechanics, Ohio State University, Columbus, March 17–19, 1952
25 Adrian R J, Meinhart C D, Tomkins C D. Vortex organization in the outer region of the turbulent boundary layer. J Fluid Mech, 2000, 422: 1–54
26 Blackwelder R F, Kaplan R E. On the wall structure of the turbulent boundary layer. J Fluid Mech, 1976, 76: 89-112
27 Ganapathisubramani B, Clemens N, Dolling D. Large-scale motions in a supersonic turbulent boundary layer. J Fluid Mech, 2006, 556: 1–11
28 Wu X H, Moin P. Forest of hairpins in a low-Reynolds-number zero-pressure-gradient flat-plate boundary layer. Phys Fluids, 2009, 21: 091106